

TECHNICAL  
REPORTS:  
METHODS

10.1002/2014JA020769

## Supporting Information:

- Text S1
- Readme

## Correspondence to:

R. H. Varney,  
rvarney@ucar.edu

## Citation:

Varney, R. H., M. Wiltberger, and W. Lotko (2015), Modeling the interaction between convection and nonthermal ion outflows, *J. Geophys. Res. Space Physics*, 120, 2353–2362, doi:10.1002/2014JA020769.

Received 26 OCT 2014

Accepted 13 FEB 2015

Accepted article online 24 FEB 2015

Published online 19 MAR 2015

## Modeling the interaction between convection and nonthermal ion outflows

R. H. Varney<sup>1</sup>, M. Wiltberger<sup>1</sup>, and W. Lotko<sup>2</sup>

<sup>1</sup>High Altitude Observatory, National Center for Atmospheric Research, Boulder, Colorado, USA, <sup>2</sup>Thayer School of Engineering, Dartmouth College, Hanover, New Hampshire, USA

**Abstract** Initial demonstrations of an ionosphere/polar wind model including a phenomenological treatment of transverse heating by wave particle interactions (WPIs) are presented. Tests with fixed WPI parameters in a designated heating region on the dayside with time-varying convection show that the parameters of the resulting nonthermal ion outflow are strongly coupled to the convection. The hemispheric outflow rate is positively correlated with the convection speed with a time delay related to the travel time to the upper boundary. Increases in convection increase the thermal plasma access to the heating region, both by increasing the upflow associated with frictional heating and by increasing the horizontal transport. The average parallel velocities and energies of the escaping nonthermal ions are anticorrelated with the convection speed due to the finite dwell time in the heating region. The computationally efficient model can be readily coupled into global geospace modeling frameworks in the future.

## 1. Introduction

The mechanisms that allow heavy ions to escape the ionosphere continue to be an active area of research (see *Yau and André* [1997]; *Yau et al.* [2011], for reviews). The recent advent of multifluid MHD models has demonstrated that this ionospheric plasma can have substantial effects on magnetospheric dynamics [e.g., *Winglee et al.*, 2002; *Wiltberger et al.*, 2010; *Yu and Ridley*, 2013]. A compelling question is what roles heavy ion outflow can play in magnetosphere-ionosphere feedback loops. Work with the multifluid Lyon-Fedder-Mobarry model [*Brambles et al.*, 2011, 2013; *Ouellette et al.*, 2013] has suggested that causally driven ion outflow forms part of a feedback loop in the development of sawtooth oscillations. These simulations use empirical relationships between O<sup>+</sup> outflow flux and DC or AC Poynting flux derived from FAST measurements to causally regulate the outflow at the inner boundary [*Strangeway et al.*, 2005; *Brambles et al.*, 2011]. These empirical relationships have several limitations. First, they are local relationships and thus cannot account for spatiotemporal lags between the magnetospheric inputs and the outflow. Second, they only give the number flux; other fluid moments are set to constants. Third, the ions enter the inner boundary of the magnetospheric simulation without any consideration of the flux the ionosphere is able to supply.

To date, the only polar wind model that has been two-way coupled to a magnetospheric MHD model is Polar Wind Outflow Model (PWOM) [*Glocer et al.*, 2009], a classical polar wind model with no transverse acceleration mechanisms. Nonetheless, PWOM produces enough O<sup>+</sup> outflow to have significant effects on the ring current, cross-polar cap potential, and the shape of the magnetosphere [*Welling et al.*, 2011; *Welling and Zaharia*, 2012]. Kinetic macroscopic particle-in-cell polar wind models have been created [e.g., *Barakat and Schunk*, 2006; *Zeng and Horwitz*, 2007], but the reliability of these models is still limited by the reliability of their inputs. In particular, the wave intensities needed to compute the transverse heating rates associated with WPI are specified empirically [*Barakat and Schunk*, 2001]. Embedding self-consistent first-principle models of the coupled wave and particle dynamics in a global simulation remains impractical at this time due to the disparate temporal and spatial scales involved. The model introduced in this report uses a phenomenological approach to WPI with tunable parameters and is sufficiently computationally efficient to be two-way coupled into global geospace modeling frameworks in the future. Simulations with the model are presented to demonstrate its behavior and sensitivity to inputs.

## 2. Model Description

The 3-D ionosphere/polar wind model (IPWM) used for this study is an extension of the 1-D model introduced by *Varney et al.* [2014]. It solves eight-moment transport equations for thermal  $H^+$ ,  $He^+$ , and  $O^+$  ( $^4S$ ) ions and only photochemistry for  $N^+$ ,  $O^+$  ( $^2D$ ),  $O^+$  ( $^2P$ ),  $NO^+$ ,  $N_2^+$ , and  $O_2^+$ . The transport is performed on a nonorthogonal magnetic-centered dipole Eulerian grid defined by altitude, L shell, and magnetic local time (MLT) coordinates. The lower and upper boundaries are spherical sections at 97 and 8400 km altitude, respectively. The low-latitude boundary at  $L = 4$  is a hard wall; plasma transport from midlatitudes is ignored. The colatitude resolution at 100 km altitude is  $\sim 1^\circ$ . The supporting information of this report gives more details on the transport equations, grid, and numerics.

Distributions of high-latitude convection and electron precipitation are provided by the Lyon-Fedder-Mobarry magnetosphere-ionosphere exchange (LFM-MIX) model via a one-way coupling. The magnetosphere-ionosphere exchange (MIX) module [*Wiltberger et al.*, 2009; *Merkin and Lyon*, 2010] is the portion of the Lyon-Fedder-Mobarry (LFM) magnetospheric MHD model [*Lyon et al.*, 2004] that handles the electrodynamic coupling between the magnetosphere and ionosphere. IPWM takes neutral densities and temperatures from NRLMSISE-00 empirical thermospheric model [*Picone et al.*, 2002]. The neutral winds are set to zero. Imposing a convection pattern but ignoring the neutral winds means that IPWM will usually overestimate the ion-neutral frictional heating [c.f. *Thayer and Semeter*, 2004]. Occasionally, winds can be produced in the direction opposite the convection, in which case ignoring the winds results in an underestimate of the frictional heating [e.g., *Carlson et al.*, 2012]. The precipitation inputs from MIX are used with a parametrization of electron impact ionization to produce ionization rates [*Fang et al.*, 2008].

For simplicity, the kinetic suprathermal electron transport model is disabled. The suprathermal electron moments are set to zero, and the photoelectron heating rate as well as the auroral electron heating rates are computed using the phenomenological model from the SAMI2 ionospheric model [*Huba et al.*, 2000]. The field-aligned currents (FACs) are ignored when computing the thermal electron velocities. In upward FAC regions the FAC is primarily carried by precipitating electrons so this assumption does not introduce serious errors. This assumption does, however, neglect upward electron velocities and associated adiabatic cooling in downward FAC regions.

IPWM includes an extra ion fluid to represent nonthermal  $O^+$ . Separating the thermal and nonthermal populations makes it easy to treat a nonthermal population that is a tiny fraction of the total  $O^+$  density, a case that is commonly observed [e.g., *Ogawa et al.*, 2008]. The transport equations obeyed by this extra fluid (see supporting information) are as follows:

$$\frac{\partial}{\partial t} n_j + \nabla \cdot [n_j \mathbf{u}_j] = \Upsilon n_j \quad (1)$$

$$\frac{\partial}{\partial t} (n_j u_{\parallel j}) + \nabla \cdot [n_j u_{\parallel j} \mathbf{u}_j] = n_j \left( \frac{e}{m_j} E_{\parallel} + g_{\parallel} + \mathbf{u}_j \mathbf{u}_j : \nabla \hat{\mathbf{b}} \right) - \frac{p_{\perp j}}{m_j} \nabla_{\parallel} \ln B + \Upsilon n_j u_{\parallel j} \quad (2)$$

$$\frac{\partial}{\partial t} \epsilon_j + \nabla \cdot [\epsilon_j \mathbf{u}_j] - \frac{p_{\perp j}}{m_j} \mathbf{u}_{\perp} \cdot \nabla_{\perp} \ln B = n_j u_{\parallel j} \left( \frac{e}{m_j} E_{\parallel} + g_{\parallel} + \mathbf{u}_j \mathbf{u}_j : \nabla \hat{\mathbf{b}} \right) + \Upsilon \epsilon_j + \frac{1}{m_j} W_{\perp} n_j. \quad (3)$$

In these equations  $n_j$ ,  $u_{\parallel j}$ ,  $p_{\perp j}$ , and  $\epsilon_j = n_j u_{\parallel j}^2 / 2 + p_{\perp j} / m_j$  are the number density, parallel velocity, perpendicular pressure, and energy density per unit mass of nonthermal  $O^+$  and  $n_i$ ,  $u_{\parallel i}$ , and  $\epsilon_i = n_i u_{\parallel i}^2 / 2 + (3/2) p_i / m_i$  are the corresponding quantities for thermal  $O^+$ . The vector velocity is  $\mathbf{u}_j = u_{\parallel j} \hat{\mathbf{b}} + \mathbf{E} \times \mathbf{B} / B^2$ . The first group of terms on the right-hand side (RHS) of (2) represents the ambipolar electric field, gravity, and the centrifugal forces. The number densities and number fluxes of the nonthermal fluid are included in the quasineutrality and current continuity conditions (see supporting information); this ensures that the self-consistent ambipolar electric field responds to the nonthermal fluid. The term on the RHS of (2) that is proportional to  $\nabla_{\parallel} \ln B$  is mirror force lifting. These equations are in the form of conservation laws with source terms and thus can be solved with the same numerical methods used for the thermal plasma transport equations. The parallel pressure, heat flow tensor, and all higher-order moments of the nonthermal fluid are neglected in this formulation; it is the lowest-order approximation which retains transverse acceleration and mirror force lifting. Neglecting these higher-order moments is tantamount to assuming all the nonthermal particles have the same energy and pitch angle. This approach ignores the population of particles that are nonthermal but

are below the mean energy of the nonthermal distribution and not at escape energies. Note that parallel pressure and heat flow of the thermal ion fluids are still included, and these terms will absolutely affect the thermal ion upflow.

The nonthermal transport equations include several ad hoc source terms to represent WPI. The promotion rate,  $\Upsilon$ , is the rate at which ions are promoted from the thermal  $O^+$  fluid into the nonthermal fluid. The thermal  $O^+$  equations include loss terms ensuring that the act of promotion conserves number density, momentum density, and energy between the two  $O^+$  populations. In all the tests presented below  $\Upsilon$  is constant with altitude. The promotion rate could be made a function of altitude in the future, but its value near the bottom of the heating region where the density of thermal particles is largest is the most important. This model treats the promotion rate as a free parameter that is independent of the transverse heating rate and the properties of the thermal distribution, but in reality it is not. One could simulate an initially Maxwellian population of test particles subjected to WPI, compute the fraction  $f$  of particles above a threshold energy after an elapsed time  $t$ , and define  $f/t$  as an effective promotion rate. The rates estimated by such experiments would depend on the properties of the initial distribution, the energy threshold chosen, and the details of the WPI mechanism. The spatiotemporal intermittency of the WPI mechanism should also be considered when determining a promotion rate. This initial study only considers a range of promotion rates that give reasonable total outflow rates. By always including some amount of promotion we are considering a best case scenario where WPI is always effective.

The final term on the RHS of (3) represents transverse heating by waves. Following *Bouhram et al.* [2004], the perpendicular heating rate per particle as a function of geocentric radius,  $r$ , is set to

$$\dot{W}_{\perp}(r) = 0.3 \left( \frac{B(1.3 R_E)}{B(r)} \right)^{1.1} \text{ eV s}^{-1}. \quad (4)$$

This rate assumes the transverse acceleration mechanism is ion cyclotron resonance heating (ICRH) [*Crew et al.* 1990] by waves with wavelengths much longer than the ion gyroradii, which is an acceptable assumption below 10000 km altitude [*Bouhram et al.*, 2004]. This type of transverse heating represents the interaction of the particles with a spectrum of broadband extremely low frequency (BBELF) waves [e.g., *Chang et al.*, 1986; *Retterer et al.*, 1987; *André et al.*, 1990]. The power law wave spectrum is assumed to be proportional to  $\omega^{-1.1}$ . The Monte Carlo simulations from *Bouhram et al.* [2004] using  $0.3 \text{ eV s}^{-1}$  at  $1.3 R_E$  and  $\omega^{-1.1}$ , using  $1.0 \text{ eV s}^{-1}$  and  $\omega^{-0.6}$  and using  $0.1 \text{ eV s}^{-1}$  and  $\omega^{-1.7}$  all produce very similar results. Thus, we have only considered the first combination of parameters for the present study. The perpendicular heating rate increases with altitude because the ion cyclotron resonance frequency decreases with decreasing magnetic field strength.

In the simulations described below  $\Upsilon$  and  $\dot{W}_{\perp}$  are only nonzero in a designated heating region, while the nonthermal fluid moments can be nonzero outside this region due to convection. Any downward flowing nonthermal ions crossing the low-altitude boundary of the heating region are demoted into the thermal population to model collisional rethermalization.

### 3. Simulation Results

The three simulations described below use representative potential and precipitation patterns taken from a single time during an LFM-MIX simulation of the 5 April 2010 storm (Figure 1). At this time the cross-polar cap potential reached 225 kV. In the terminology of *Wahlund et al.* [1992], only type I ion upflows are important in these simulations because LFM-MIX includes monoenergetic and diffuse precipitation only, which includes little soft precipitation and is not very effective at producing electron heating and type II ion upflow.

The simulations are not intended to reproduce the 5 April 2010 event; they use March equinox,  $F_{10.7} = 140$ , and  $Ap = 3.0$  conditions for the various empirical models. The simulations are initialized 12 h before  $t = 0$  to allow transients from the initial conditions to disappear. At  $t = 0$  the WPI parameters are switched on in a designated heating region. This region extends from 10.5 to 13.5 MLT on the dayside, extends from  $z_0 = 1900 \text{ km}$  altitude up to the 8400 km upper boundary along magnetic field lines, and maps to  $80.5^\circ$  to  $82.5^\circ$  magnetic latitude at 100 km. This example region is  $\sim 5^\circ$  poleward of the typical cusp/cleft; future studies could dynamically determine the heating region using a cusp identification algorithm. The

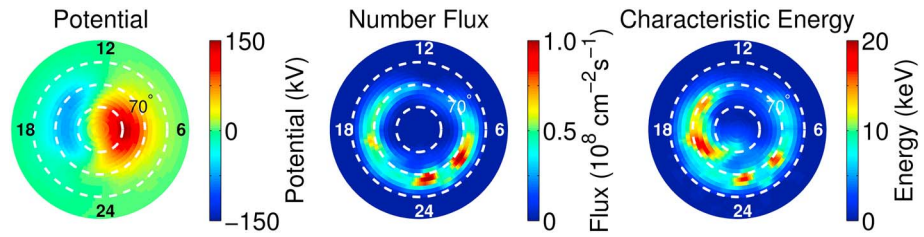


**Figure 1.** MIX input parameters mapped to 100 km altitude. The panels plot the electrostatic potential (without corotation), precipitating electron number flux, and characteristic energy. The dashed white lines are spaced 10° in magnetic colatitude. In each panel 12 MLT is at the top and 6 MLT is to the right.

vertical extent of the region is comparable to the 2000 to 8000 km altitude heating wall simulated by *Knudsen et al.* [1994]. The horizontal thickness is much larger than the 30 km wide heating wall considered by *Knudsen et al.* [1994], but comparable to the 1°–2° wide heating regions modeled by *Dubouloz et al.* [1998] and *Bouhram et al.* [2004]. After  $t = 0$  the promotion rate is set to a constant  $\Upsilon = 3 \times 10^{-3} \text{ s}^{-1}$  in the heating region. This value was chosen such that it gives a total outflow rate of  $\sim 10^{25}$  ion/s. The changes in the results with changes in  $\Upsilon$  and  $z_0$  are discussed later. For the convection pattern in Figure 1 flux tubes take roughly  $\tau = 125 \text{ s}$  to traverse the 2° heating region. This time is short compared to the 500 s residence time assumed by *Bouhram et al.* [2004] because the convection speed is so fast.

In order to investigate the variations in outflow with variations in convection, the simulations described below artificially scale the  $\mathbf{E} \times \mathbf{B}$  drifts by a time-dependent scaling factor,

$$f(t) = \begin{cases} 1 & t < 2 \text{ h} \\ 1 - \frac{0.75}{4 \text{ h}} (t - 2 \text{ h}) & 2 \text{ h} \leq t < 6 \text{ h} \\ 1 - 0.75 \cos \left[ \frac{2\pi}{2 \text{ h}} (t - 6 \text{ h}) \right] & t \geq 6 \text{ h} \end{cases} \quad (5)$$

Simulation 1 consistently uses the scaled drifts in the convection, centrifugal acceleration, and frictional heating terms. Simulations 2 and 3 are a nonself-consistent numerical experiments in which the scaled drifts are used in some terms, and the unscaled drifts are used in the other terms. Simulation 2 uses the scaled drifts in all of the terms except the frictional heating terms, and simulation 3 uses the scaled drifts in only the frictional heating terms.

All three simulations are identical through  $t = 2 \text{ h}$ . Figure 2 shows parameters of the nonthermal fluid in the noon-midnight plane at time  $t = 2 \text{ h}$  from simulation 1. Convection drags the energized ions out of the heating region and creates an ion fountain extending across the pole [c.f. *Lockwood et al.*, 1985]. The highest perpendicular energies and parallel velocities appear at the upper boundary just poleward of the heating region. The perpendicular energies downstream of the heating region become small because without the continued transverse heating, the mirror force quickly transforms perpendicular energy into parallel velocity. Although the nonthermal ions in the simulation are always outflowing, these are a small fraction of the total  $\text{O}^+$  population. The parallel velocities of the thermal  $\text{O}^+$  ions at 850 km in the simulation (not shown) are generally upward over the cusp and auroral regions and downward over the polar cap, and thus in qualitative agreement with statistics on bulk ion flows at 850 km from DMSP [*Redmon et al.*, 2010].

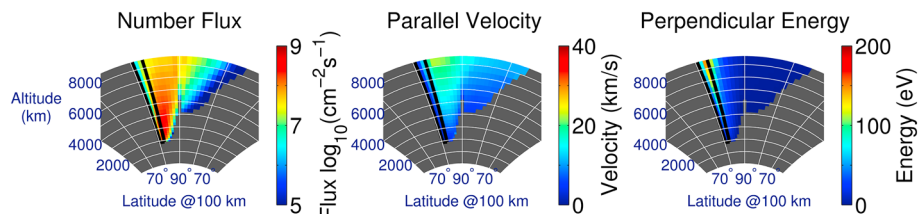


**Figure 2.** Nonthermal ion parameters in the SM XZ (noon-midnight) plane at  $t = 2 \text{ h}$ . The dayside is to the left. The thick black lines outline the heating region. Gray regions denote areas where the nonthermal ion density is zero.

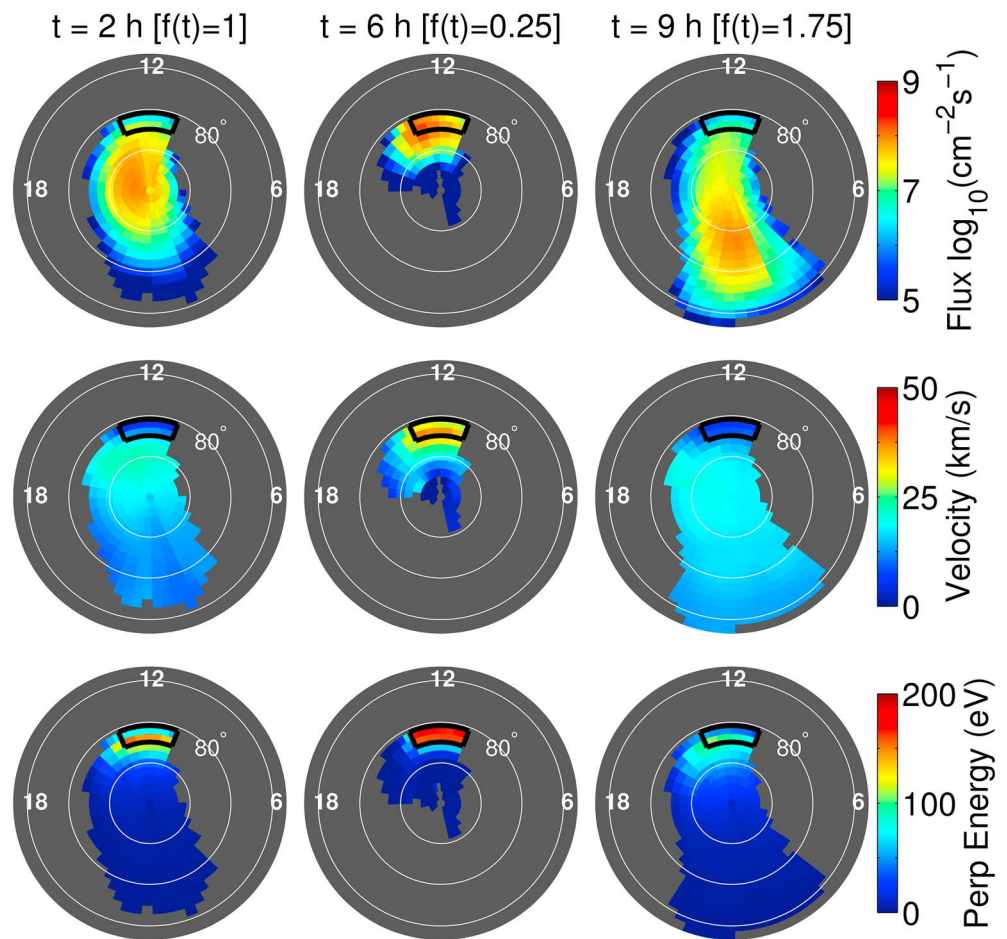


**Figure 3.** Nonthermal ion parameters at the upper boundary (8400 km) at different times (different columns) in simulation 1. (top row) The number flux; (middle row) the parallel velocity; (bottom row) the perpendicular energy per particle,  $p_{\perp j}/n_j$ . In each plot 12 MLT is at the top, 6 MLT is to the right, and the heating region is outlined in thick black lines. The thin white circles are spaced  $5^\circ$  in latitude when mapped to 100 km ( $\sim 7.5^\circ$  at 8400 km). Gray regions denote areas where the nonthermal ion density is zero. The outer boundary of each plot maps to  $73^\circ$  latitude at 100 km; the nonthermal ions never reach more equatorward parts of the simulation domain.

Figure 3 plots the nonthermal ion parameters at the upper boundary at three different times from simulation 1. Intuitively, the faster the convection, the more extended the ion fountain becomes. The region immediately downward of the heating region is unpopulated because nonthermal ions leave the upper boundary before the flux tubes complete a full rotation of the dawn convection cell. The convection pattern is such that plasma primarily enters the heating region through the equatorward and downward sides and exits through the poleward and duskward sides.

Figure 4 presents several diagnostics from the three simulations. The outflow rate plotted is the nonthermal  $O^+$  flux integrated over the entire model upper boundary. The inflow rates plotted are thermal  $O^+$  fluxes integrated over sides of the heating region. The horizontal rate is the sum of the integrals over the equatorward and downward sides. The flux through those two faces is unaffected by the heating region since flux tubes convect into the heating region from the dawnward and equatorward sides and out through the duskward and poleward sides for this particular convection pattern. The vertical rate is the integral over the bottom boundary of the heating region. For  $0 \leq t \leq 2$  h the nonthermal outflow rate is 25% of the total thermal inflow rate because many thermal ions exit the heating region before being promoted. If the vertical extent of the heating region were infinite then  $1 - e^{-Y\tau} = 31\%$  of the entering thermal ions

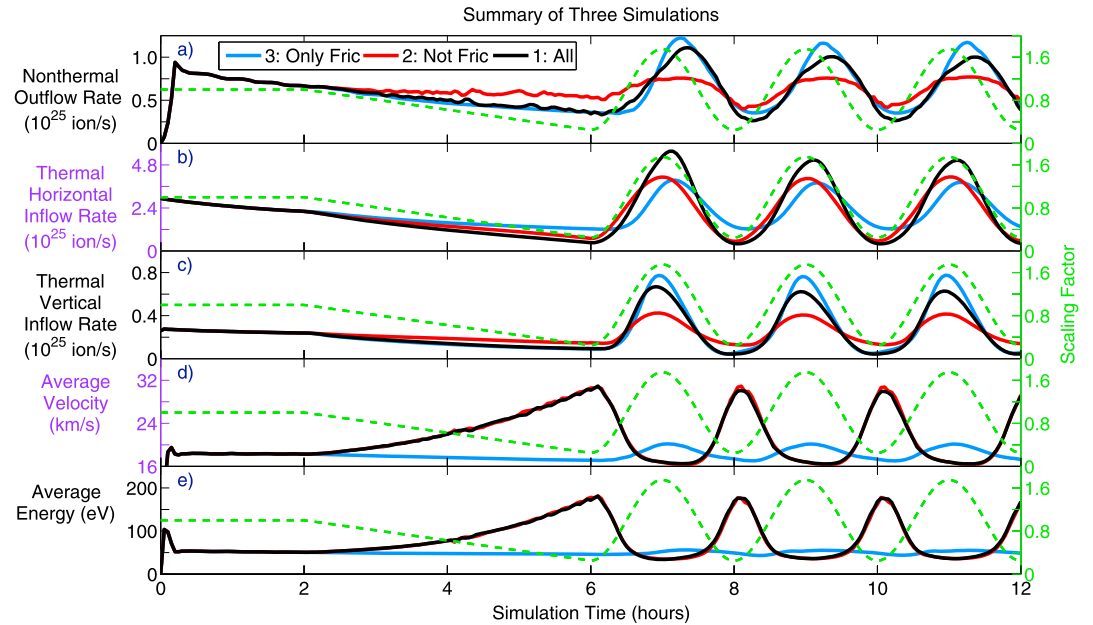


**Figure 4.** Diagnostics from the three simulations. (a) Nonthermal ion outflow rate through the entire upper boundary; (b) horizontal thermal ion inflow rate to the heating region; (c) vertical thermal ion inflow rate to the heating region; (d) flux-weighted average parallel velocities of the nonthermal ions,  $\langle u_{\parallel j} \rangle$ ; and (e) flux-weighted average energies of the nonthermal ions,  $\langle W_j \rangle$ . The scaling factor from (5),  $f(t)$ , is superimposed on each plot to guide the eye (green dashed curves).

would be promoted. Not all of the particles spend the entire 125 s in the heating region because some are entering through the bottom or leaving through the top. Finally, the flux-weighted average parallel velocities and energies plotted in Figures 4d and 4e are defined as

$$\langle u_{\parallel j} \rangle \equiv \frac{\iint n_j u_{\parallel j} \mathbf{u}_j \cdot d\mathbf{A}}{\iint n_j \mathbf{u}_j \cdot d\mathbf{A}} \quad (6)$$

$$\langle W_j \rangle \equiv \frac{\iint \left( \frac{1}{2} m_j n_j u_{\parallel j}^2 + p_{\perp j} \right) \mathbf{u}_j \cdot d\mathbf{A}}{\iint n_j \mathbf{u}_j \cdot d\mathbf{A}}, \quad (7)$$

where the surface integrals are performed over the upper boundary.

The outflow rate is positively correlated with the scaling factor in all three simulations, albeit with a time delay of  $\sim 20$  min. The correlation is readily understood in terms of plasma access to the heating region. The nonthermal outflow flux is limited by the supply of thermal ions to the heating region. In all cases the inflow rates are positively correlated with the scaling factor with varying time delays. The significant modulation of the horizontal inflow rate demonstrates that ion upflow from local frictional heating is not the only important process. The horizontal inflow rate is modulated both by modulating the drift velocity and by modulating the ion upflow into the region upstream of the heating region. Simulation 3 isolates the latter effect.

Even though the outflow rates are positively correlated with the convection scaling factor, the average parallel velocities and energies are anticorrelated with the scaling factor due to the finite dwell time of nonthermal ions in the heating region. In simulation 3, where the horizontal velocities and thus the dwell times are not being modulated, this anticorrelation disappears and is replaced by a weak correlation. The average perpendicular energies defined as  $\langle W_{\perp j} \rangle \equiv \langle W_j \rangle - \frac{1}{2} m_j \langle u_{\parallel j} \rangle^2$  (not shown) exhibit a similar anticorrelation with the scaling factor. The behaviors of parallel velocities and perpendicular energies sampled at fixed grid points are more complicated than the behaviors of the flux-weighted average quantities. Downstream from the heating region the parallel velocities and perpendicular energies at a fixed location are positively correlated with the scaling factor because the central, most energetic part of the fountain moves as the convection changes.

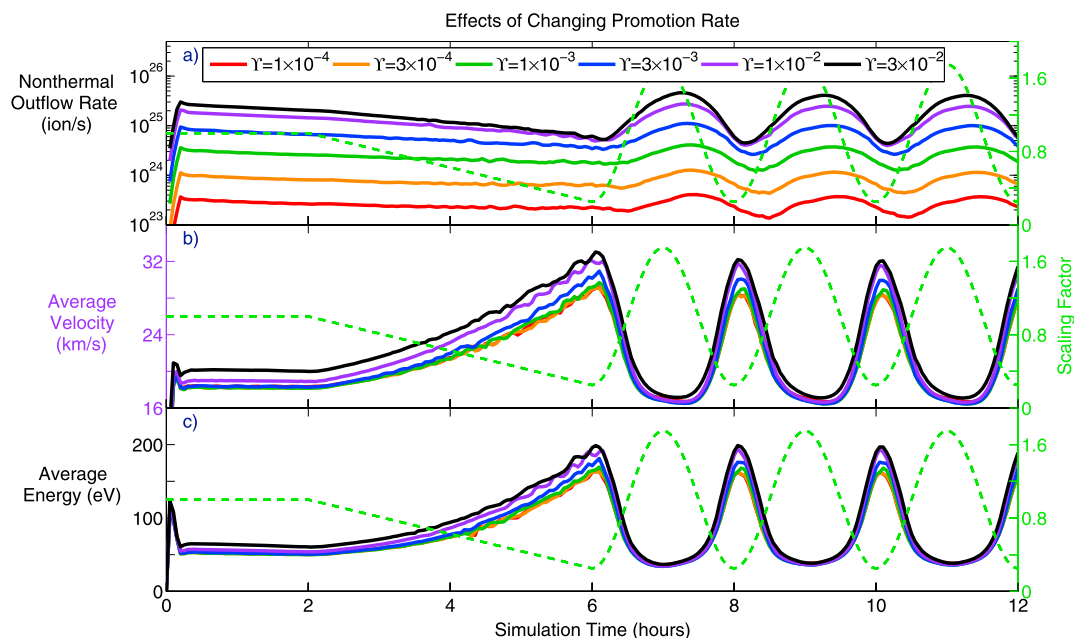


**Figure 5.** Comparison of six different simulations with different promotion rates,  $\Upsilon$ , indicated in the legend in units of  $s^{-1}$ . The  $\Upsilon = 3 \times 10^{-3} s^{-1}$  simulation is simulation 1 from Figure 4. (a) Nonthermal ion outflow rate through the entire upper boundary; (b) flux-weighted average parallel velocities of the nonthermal ions,  $\langle u_{ij} \rangle$ ; and (c) flux-weighted average energies of the nonthermal ions,  $\langle W_j \rangle$ . The scaling factor from (5),  $f(t)$ , is superimposed on each plot to guide the eye (green dashed curves).

The above simulations were performed with an arbitrarily chosen promotion rate of  $\Upsilon = 3 \times 10^{-3} s^{-1}$ . Figure 5 compares simulation 1 to otherwise identical simulations with different promotion rates. The time-delayed correlation between convection velocity and hemispheric outflow rate and the anticorrelation between convection and average velocity/energy are observed in all of these simulations. By virtue of conservation, in steady state the hemispheric outflow rate equals the promotion rate times the total thermal  $O^+$  density in the heating region. At low values of  $\Upsilon$  the process of promotion does not significantly deplete the thermal population in the heating region, and thus, hemispheric outflow rate increases linearly with  $\Upsilon$ . At higher values of  $\Upsilon$  the depletion of the thermal population in the heating region limits the outflow rate. The outflow flux is limited by the amount of plasma the lower ionosphere can supply to the heating region. The flux limiting by the lower ionosphere is most significant above  $\Upsilon = 10^{-2} s^{-1}$ .

The average velocities and energies are comparable across 2 orders of magnitude of variation in the promotion rate, and comparisons of individual profiles of velocity and energy show similar behavior. If noninteracting test particles were simulated, the velocities and energies achieved would be completely independent of the number of particles being simulated. In these simulations, however, the self-consistent ambipolar electric field introduces collective effects. In high  $\Upsilon$  cases the larger depletions of the high-altitude densities create larger density gradients between low and high altitudes, and hence larger upward ambipolar fields. The parallel acceleration from these fields cause the velocities to increase slightly with increasing  $\Upsilon$ . The distance a particle travels across the polar cap before exiting the simulation domain through the upper boundary depends on the ratio between the convection velocity and the parallel velocity. The simulations have identical convection velocities and similar parallel velocities, and thus, the spatial extent and morphology of the resulting ion fountains are nearly independent of the promotion rate.

Additional tests were performed to address the sensitivity of the results to the altitude  $z_0$  of the lower boundary of the heating region, and these tests are summarized in Figure 6. Each of these tests is identical to simulation 1 in Figure 4 except for the choice of  $z_0$ . The transverse heating rate is always set according to (4) even when  $1.3 R_E$  is not the lower boundary of the heating region. The hemispheric outflow rate increases substantially with decreasing  $z_0$  both because the volume of the heating region increases and the thermal  $O^+$  density increases exponentially with decreasing altitude. The flux-weighted average velocities and energies decrease with decreasing  $z_0$  because a larger fraction of the total flux is coming

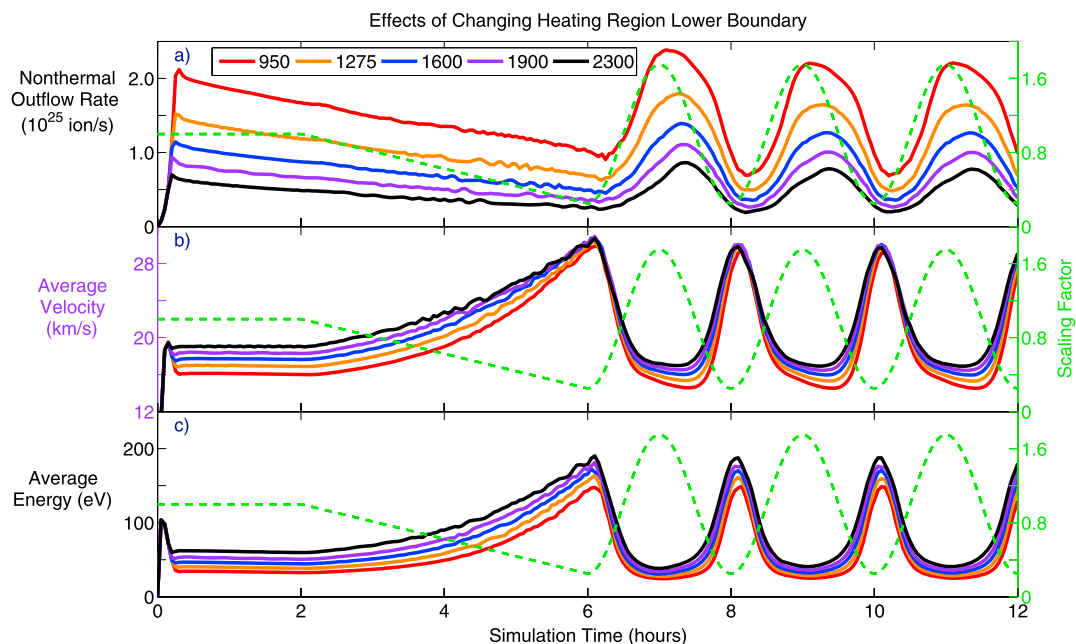


**Figure 6.** Comparison of five different simulations with lower altitude boundaries of the heating region,  $z_0$ , indicated in the legend in kilometers. The  $z_0 = 1900$  km simulation is simulation 1 from Figure 4. (a) Nonthermal ion outflow rate through the entire upper boundary; (b) flux-weighted average parallel velocities of the nonthermal ions,  $\langle u_{\parallel} \rangle$ ; and (c) flux-weighted average energies of the nonthermal ions,  $\langle W_j \rangle$ . The scaling factor,  $f(t)$ , is superimposed on each plot to guide the eye (green dashed curves).

from lower altitudes where the transverse heating rate per particle is smaller. Analysis of the morphology of the ion fountain produced shows that the extent of the fountain across the polar cap increases with decreasing  $z_0$ .

#### 4. Conclusions

This report presents first results from IPWM, which includes nonthermal  $O^+$  ions obeying the simplest set of transport equations that includes the combined effects of transverse acceleration and mirror force lifting. Determining an optimal tuning for the WPI terms is complicated, however, because the nonthermal ion outflow produced by IPWM depends on many other parameters. The simulations presented here demonstrate that even with the WPI parameters held constant, the properties of the nonthermal outflow vary substantially with variations in the convection. The convection transports the nonthermal ions out of the heating region creating an ion fountain whose extent depends on the convection speed [Lockwood *et al.*, 1985]. The hemispheric outflow rate is positively correlated with the convection speed due to effects involving plasma access to the heating region, whereas the flux-weighted average parallel velocities and energies are anticorrelated with the convection speed due to a dwell time effect. Qualitatively, these correlations are robust to the changes of the promotion rate,  $\Upsilon$ , and lower boundary of the heating region,  $z_0$ .

Unlike local empirical outflow relationships, IPWM exhibits spatiotemporal lags and correlations between the outflow and its drivers. The time delay of  $\sim 20$  min between changes in convection and changes in the hemispheric outflow rate is comparable to the time it takes a particle with an average vertical velocity of 5 km/s to travel the 6500 km vertical extent of the heating region. The modulation of the outflow rate with changes in convection is not entirely controlled by upflow into the heating region; horizontal transport of plasma into the heating region is also important. Thus, changes in ion upflow on flux tubes upstream of the heating region can affect the ion outflow that is ultimately produced.

IPWM also provides moments of the nonthermal fluid other than just the number flux, and these moments vary dynamically with changes in the driving. The largest parallel velocities and perpendicular energies appear just poleward of the heating region. The variations in these other parameters are just as important as

variations in the hemispheric outflow rate because these parameters affect the trajectories of these particles in the magnetosphere. In idealized multifluid MHD simulations with specified cusp outflow, both *Wiltberger et al.* [2010] and *Yu and Ridley* [2013] observed that the magnitudes of the outflow fluxes are not enough to determine the outflow's influence on magnetotail dynamics. The parallel velocity and energy influence where the outflow will land down the tail, and the landing location is crucially important to determining the effects of the outflow.

The initial demonstration of IPWM presented here can be improved in several ways. The effects of soft (few 100 eV) electron precipitation on electron heating and type II upflow [*Wahlund et al.*, 1992] in the cusp can be studied using LFM's recently implemented direct-entry and broadband precipitation models [*Zhang et al.*, 2012]. The magnitude and distribution of the ad hoc source terms representing WPI can be causally regulated by electromagnetic energy flows from the magnetosphere, e.g., using the simulated Alfvénic Poynting flux flowing to low altitude [*Brambles et al.*, 2011]. ICRH by BBELF in the dayside cusp region is only one type of ion acceleration producing nonthermal ion outflows. In principle this model could be extended to include heating in other regions, such as the nightside auroral oval and use different prescriptions for the transverse heating rate in the different regions to represent a variety of acceleration processes. For example, interactions with dispersive Alfvén waves and other waves below the ion gyrofrequency can be important [e.g., *Chaston et al.*, 2004; *Temerin and Roth*, 1986]. Lack of empirical knowledge of how low in altitude transverse heating is initiated, to some extent, undermines the application of models for transversely heated ions, like the one proposed here. Nevertheless, the model can be used to explore reasonable limits on the altitude distribution and rates of acceleration for different multistage processes. Despite its limitations, the fluid-like nature of the model makes it computationally efficient relative to particle simulations. At the resolution presented here the model runs at approximately 3 times real time on 32 processors. The fixed, Eulerian grid means that in order to pass outflow from IPWM to a magnetospheric magnetohydrodynamics model like LFM, interpolation coefficients only need to be computed once. Thus, the IPWM can be readily coupled into a global geospace modeling framework to provide a dynamic and causal source of ion outflow.

#### Acknowledgments

The National Center for Atmospheric Research (NCAR) is sponsored by the National Science Foundation. R.H.V. is supported by the NASA Living With a Star Jack Eddy Postdoctoral Fellowship Program, administered by the University Corporation for Atmospheric Research and NSF grant AGS-1400985. M.W. and W.L. are supported by NASA grants NNX11AO59G and NNX11AJ10G. The model source code, output, and analysis routines used in this report will be preserved on a long-term storage system at NCAR and made available upon request to the corresponding author.

Michael Liemohn thanks the reviewers for their assistance in evaluating this paper.

#### References

- André, M., G. B. Crew, W. K. Peterson, A. M. Persoon, C. J. Pollock, and M. J. Engebretson (1990), Ion heating by broadband low-frequency waves in the cusp/cleft, *J. Geophys. Res.*, *95*, 20,809–20,823.
- Barakat, A. R., and R. W. Schunk (2001), Effects of wave–particle interactions on the dynamic behavior of the generalized polar wind, *J. Atmos. Sol. Terr. Phys.*, *63*, 75–83.
- Barakat, A. R., and R. W. Schunk (2006), A three-dimensional model of the generalized polar wind, *J. Geophys. Res.*, *111*, A12314, doi:10.1029/2006JA011662.
- Bouhram, M., B. Klecker, W. Miyake, H. Rème, J.-A. Sauvaud, M. Malingre, L. Kistler, and A. Blågåu (2004), On the altitude dependence of transversely heated O<sup>+</sup> distributions in the cusp/cleft, *Ann. Geophys.*, *22*, 1787–1798.
- Brambles, O. J., W. Lotko, B. Zhang, M. Wiltberger, J. Lyon, and R. J. Strangeway (2011), Magnetosphere sawtooth oscillations induced by ionospheric outflow, *Science*, *332*(6034), 1183, doi:10.1126/science.1202869.
- Brambles, O. J., W. Lotko, B. Zhang, J. Ouellette, J. Lyon, and M. Wiltberger (2013), The effects of ionospheric outflow on CME and SIR driven sawtooth events, *J. Geophys. Res. Space Physics*, *118*, 6026–6041, doi:10.1002/jgra.50522.
- Carlson, H. C., T. Spain, A. Aruliah, A. Skjaeveland, and J. Moen (2012), First-principles physics of cusp/polar cap thermospheric disturbances, *Geophys. Res. Lett.*, *39*, L19103, doi:10.1029/2012GL053034.
- Chang, T., G. B. Crew, H. Hershkovitz, J. R. Jasperse, and J. M. Retterer (1986), Transverse acceleration of oxygen ions by electromagnetic ion cyclotron resonance with broadband left-hand-polarized waves, *Geophys. Res. Lett.*, *13*, 636–639.
- Chaston, C. C., J. W. Bonnell, C. W. Carlson, J. P. McFadden, R. E. Ergun, R. J. Strangeway, and E. J. Lund (2004), Auroral ion acceleration in dispersive Alfvén waves, *J. Geophys. Res.*, *109*, A04205, doi:10.1029/2003JA010053.
- Crew, G. B., T. Chang, J. M. Retterer, W. K. Peterson, D. A. Gurnett, and R. L. Huff (1990), Ion cyclotron resonance heated conics: Theory and observations, *J. Geophys. Res.*, *95*(A4), 3959–3985.
- Dubouloz, N., D. Delcourt, M. Malingre, J.-J. Berthelier, and D. Chugunin (1998), Remote analysis of cleft ion acceleration using thermal plasma measurements from Interball Auroral Probe, *Geophys. Res. Lett.*, *25*, 2925–2928.
- Fang, X., C. E. Randall, D. Lummerzheim, S. C. Solomon, M. J. Mills, D. R. Marsh, C. H. Jackman, W. Wang, and G. Lu (2008), Electron impact ionization: A new parameterization for 100 eV to 1 MeV electrons, *J. Geophys. Res.*, *113*, A09311, doi:10.1029/2008JA013384.
- Glocer, A., G. Tóth, T. Gombosi, and D. Welling (2009), Modeling ionospheric outflows and their impact on the magnetosphere, initial results, *J. Geophys. Res.*, *114*, A05216, doi:10.1029/2009JA014053.
- Huba, J. D., G. Joyce, and J. A. Fedder (2000), Sami2 is Another Model of the Ionosphere (SAMI2): A new low-latitude ionosphere model, *J. Geophys. Res.*, *105*(A10), 23,035–23,053.
- Knudsen, D. J., B. A. Whalen, T. Abe, and A. Yau (1994), Temporal evolution and spatial dispersion of ion conics: Evidence of a polar cusp heating wall, in *Solar System Plasmas in Space and Time*, *Geophys. Monogr. Ser.*, vol. 84, edited by J. L. Burch and J. H. Waite Jr., pp. 163–169, AGU, Washington, D. C.
- Lockwood, M., M. O. Chandler, J. L. Horwitz, J. H. Waite Jr., T. E. Moore, and C. R. Chappell (1985), The cleft ion fountain, *J. Geophys. Res.*, *90*, 9736–9748.
- Lyon, J. G., J. A. Fedder, and C. M. Mobarry (2004), The Lyon-Fedder-Mobarry (LFM) global MHD magnetospheric simulation code, *J. Atmos. Sol. Terr. Phys.*, *66*, 1333–1350, doi:10.1016/j.jastp.2004.02.020.

- Merkin, V. G., and J. G. Lyon (2010), Effects of the low-altitude ionospheric boundary condition on the global magnetosphere, *J. Geophys. Res.*, *115*, A10202, doi:10.1029/2010JA015461.
- Ogawa, Y., et al. (2008), Coordinated EISCAT Svalbard radar and Reimei satellite observations of ion upflows and suprathermal ions, *J. Geophys. Res.*, *113*, A05306, doi:10.1029/2007JA012791.
- Ouellette, J. E., O. J. Brambles, J. G. Lyon, W. Lotko, and B. N. Rogers (2013), Properties of outflow-driven sawtooth substorms, *J. Geophys. Res. Space Physics*, *118*, 3223–3232, doi:10.1002/jgra.50309.
- Picone, J. M., A. E. Hedin, D. P. Drob, and A. C. Aikin (2002), NRLMSISE-00 empirical model of the atmosphere: Statistical comparisons and scientific issues, *J. Geophys. Res.*, *107*(A12), 1468, doi:10.1029/2002JA009430.
- Redmon, R. J., W. K. Peterson, L. Andersson, E. A. Kihn, W. F. Denig, M. Hairston, and R. Coley (2010), Vertical thermal O<sup>+</sup> flows at 850 km in dynamic auroral boundary coordinates, *J. Geophys. Res.*, *115*, A00J08, doi:10.1029/2010JA015589.
- Retterer, J. M., T. Chang, G. B. Crew, J. R. Jasperse, and J. D. Winningham (1987), Monte Carlo modeling of ionospheric oxygen acceleration by gyrotron resonance with broad-band electromagnetic turbulence, *Phys. Rev. Lett.*, *59*, 148.
- Strangman, R. J., R. E. Ergun, Y.-J. Su, C. W. Carlson, and R. C. Elphic (2005), Factors controlling ionospheric outflows as observed at intermediate altitudes, *J. Geophys. Res.*, *110*, A03221, doi:10.1029/2004JA010829.
- Temerin, M., and I. Roth (1986), Ion heating by waves with frequencies below the ion gyrofrequency, *Geophys. Res. Lett.*, *13*(11), 1109–1112.
- Thayer, J. P., and J. Semeter (2004), The convergence of magnetospheric energy flux in the polar atmosphere, *J. Atmos. Sol. Terr. Phys.*, *66*, 807–817, doi:10.1016/j.jastp.2004.01.035.
- Varney, R. H., S. C. Solomon, and M. J. Nicolls (2014), Heating of the sunlit polar cap ionosphere by reflected photoelectrons, *J. Geophys. Res. Space Physics*, *119*, 8660–8684, doi:10.1002/2013JA019378.
- Wahlund, J.-E., H. J. Oppenorth, I. H. K. J. Winsor, and G. O. L. Jones (1992), EISCAT observations of topside ionospheric ion outflows during auroral activity: Revisited, *J. Geophys. Res.*, *97*(A3), 3019–3037.
- Welling, D. T., and S. G. Zaharia (2012), Ionospheric outflow and cross polar cap potential: What is the role of magnetospheric inflation?, *Geophys. Res. Lett.*, *39*, L23101, doi:10.1029/2012GL054228.
- Welling, D. T., V. K. Jordanova, S. G. Zaharia, A. Glocer, and G. Tóth (2011), The effects of dynamic ionospheric outflow on the ring current, *J. Geophys. Res.*, *116*, A00J19, doi:10.1029/2010JA015642.
- Wiltberger, M., R. S. Weigel, W. Lotko, and J. A. Fedder (2009), Modeling seasonal variations of auroral particle precipitation in a global-scale magnetosphere-ionosphere simulation, *J. Geophys. Res.*, *114*, A01204, doi:10.1029/2008JA013108.
- Wiltberger, M., W. Lotko, J. G. Lyon, P. Damiano, and V. Merkin (2010), Influence of cusp O<sup>+</sup> outflow on magnetotail dynamics in a multifluid MHD model of the magnetosphere, *J. Geophys. Res.*, *115*, A00305, doi:10.1029/2010JA015579.
- Winglee, R. M., D. Chua, M. Brittnacher, G. K. Parks, and G. Lu (2002), Global impact of ionospheric outflows on the dynamics of magnetosphere and cross-polar cap potential, *J. Geophys. Res.*, *107*(A9), 1237, doi:10.1029/2001JA000214.
- Yau, A. W., and M. André (1997), Sources of ion outflow in the high latitude ionosphere, *Space Sci. Rev.*, *80*, 1–25.
- Yau, A. W., W. K. Peterson, and T. Abe (2011), Influences of the ionosphere, thermosphere and magnetosphere on ion outflows, in *The Dynamic Magnetosphere, IAGA Spec. Sopron Book Ser.*, vol. 3, edited by A. W. Yau, W. K. Peterson, and T. Abe, pp. 283–314, Springer, Netherlands, doi:10.1007/978-94-007-0501-2\_16.
- Yu, Y., and A. J. Ridley (2013), Exploring the influence of ionospheric O<sup>+</sup> outflow on magnetospheric dynamics: Dependence on the source location, *J. Geophys. Res. Space Physics*, *118*, 1711–1722, doi:10.1029/2012JA018411.
- Zeng, W., and J. L. Horwitz (2007), Formula representation of auroral ionospheric O<sup>+</sup> outflows based on systematic simulations with effects of soft electron precipitation and transverse ion heating, *Geophys. Res. Lett.*, *34*, L06103, doi:10.1029/2006GL028632.
- Zhang, B., W. Lotko, O. Brambles, P. Damiano, M. Wiltberger, and J. Lyon (2012), Enhancement of thermospheric mass density by soft electron precipitation, *Geophys. Res. Lett.*, *39*, L20102, doi:10.1029/2012GL053519.